scientific reports

OPEN

Cenozoic evolution of earth's strongest geoid low illuminates mantle dynamics beneath Antarctica

Petar Glišović[1,2,3] ✉ & Alessandro M. Forte[1,3,4]

Constraining the long-term evolution of geoid anomalies is essential for unraveling Earth's internal dynamics. While most studies focus on present-day geoid snapshots, we reconstruct the time-dependent evolution of Earth's strongest geoid depression, the Antarctic Geoid Low (AGL), over the Cenozoic. Unlike geodetic reference frames that place the deepest geoid low in the Indian Ocean, a geodynamic perspective – relative to a hydrostatic ellipsoid – reveals the strongest nonhydrostatic geoid depression resides over Antarctica. Using a back-and-forth nudging technique for time-reversed mantle convection modeling, we leverage 3-D mantle density structures derived from seismic tomography and geodynamic constraints. Our results show that the AGL has persisted for at least ~70 Myr, undergoing a major transition in amplitude and position between 50 and 30 Ma. This transition coincides with an abrupt lateral shift in Earth's rotation axis at ~50 Ma, independently validated through paleomagnetic constraints on True Polar Wander. Initially, the AGL was supported by stable lower mantle density anomalies, but over the past ~40 Myr, an increasing contribution from upper-mantle buoyancy – particularly above ~1300 km depth – amplifie the AGL magnitude. This shift reflect the interplay between long-term deep subduction beneath the Northwest Antarctic margin and a broad, thermally driven upwelling of buoyant material sourced from the lowermost mantle. These results contrast with earlier interpretations by demonstrating the crucial role of time-dependent coupling between both positive and negative mantle buoyancy in shaping global geoid anomalies. By integrating seismic, geodynamic, and mineral-physics data, our reconstructions provide a dynamically consistent view of mantle flo beneath Antarctica and offe new insights into the coupling between deep and shallow mantle processes that govern Earth's long-wavelength geoid evolution.

A discrepancy in the defin tion of geoid anomalies between the space geodetic and geodynamics communities has caused confusion regarding their amplitude, geometry, and dynamic origins. Most previous geodynamic modelling studies have concentrated on matching the present-day geoid, offering only a static snapshot of mantle conditions. In contrast, we reconstruct the long-term evolution of the geoid over the past 70 million years, clarifying the time-dependent origin of the deepest geoid low on our planet and thereby elucidating the connections between deep mantle processes, surface observables, and Earth's rotational behaviour throughout the Cenozoic. We present critical tests of the realism of Earth's predicted internal dynamics by comparing the predicted degree-2 component of the geoid variation against estimated True Polar Wander (TPW) trajectories derived from paleomagnetic data. Th s independent validation substantiates the reliability of our mantle fl w reconstructions, in particular their ability to predict a realistic temporal evolution of the geoid variations.

The geodetically defi ed global geoid undulations[1,2] are referenced to the WGS84 ellipsoid[3], in which the strongest geoid low is located in the Indian Ocean (Fig. 1A), and this geodetic representation has been employed as a constraint on Earth's internal structure and dynamics in some geodynamic studies[4,5]. However, it is crucial to recognize that the observed ellipticity of Earth's gravitational figu e encompasses a substantial component originating from Earth's internal dynamics, which also drive tectonic plate motions in addition to the geoid anomalies.

[1]Équipe de Géomagnétisme, Institut de Physique du Globe de Paris, Paris, France. [2]Department of Geological Sciences and Geological Engineering, Queen's University, Kingston, ON K7L 3N6, Canada. [3]GEOTOP, Université du Québec à Montréal, Montréal, QC H3C 3P8, Canada. [4]Department of Geological Sciences, University of Florida, Gainesville, FL 32611, United States of America. ✉email: pglisovic@gmail.com

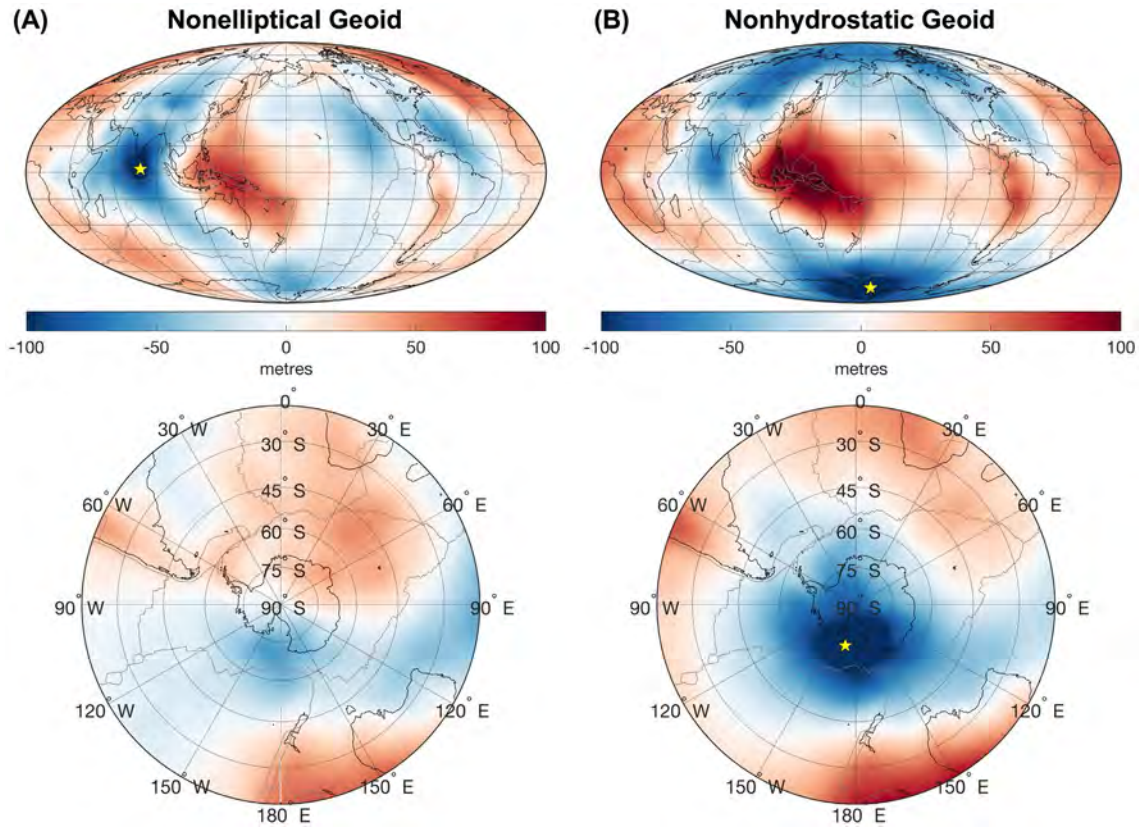

Fig. 1. Present-day geoid anomalies. (**A**) Nonelliptical geoid undulations, derived from the GRACE geopotential, but represented relative to the WGS84 reference ellipsoid[3]. (**B**) Nonhydrostatic geoid undulations derived from the GRACE geopotential solution[2] relative to Earth's hydrostatic ellipsoidal figu e, arising from the diurnal rotation[6]. The upper maps displays global geoid anomalies, while the lower maps focus on geoid anomalies above Antarctica and its surrounding regions. In all cases, the geoid undulations are calculated from a spherical harmonic representation of the GRACE geopotential truncated at harmonic degree $\ell = 32$. The yellow star marks the geographic location of Earth's deepest geoid depression on the nonhydrostatic and nonelliptical geoid, respectively. The black and grey lines display the present-day position of the plate boundaries and coastlines.

Th s internal dynamical contribution to Earth's elliptical shape explains why geodynamicists use a hydrostatic reference ellipsoid to defi e geoid undulations. Th s hydrostatic ellipsoid represents the theoretically predicted flattening of Earth's gravitational figu e due only to its diurnal rotation, in which all internal dynamics are absent[6]. Subtracting the hydrostatic ellipticity from the observed geoid yields the so-called "nonhydrostatic" geoid undulations (Fig. 1B). In this nonhydrostatic geoid, the strongest geoid low on our planet is over Antarctica, not over the Indian Ocean as in the common geodetic representation of the anomalous (non-elliptical) geoid. The Earth's strongest nonhydrostatic geoid low sits directly over the Ross Sea, in the marine sector of the Ross Embayment, between Victoria Land and Marie Byrd Land (Fig. 1B).

The Earth's nonhydrostatic gravitational fi ld provides a critical constraint on mantle density anomalies and their dynamic evolution[7,8]. Th s signifi ance was recognized since the advent of the earliest seismic images of global-scale heterogeneity in the mantle[9], which revealed that the long-wavelength heterogeneity in the deep mantle is strongly correlated with the undulations of the nonhydrostatic geoid. Specifi ally, regions of heightened geoid elevations align with deep-mantle regions featuring low-velocity anomalies, and conversely, areas of geoid depressions correspond with elevated-velocity zones[10–13]. Th s correlation has been the focus of signifi ant scientific attention over the past four decades because of its critical importance for understanding the geodynamic evolution in Earth's deep interior.

For instance, past analyses of the relationship between present-day geoid anomalies and geological reconstructions of past configur tions of tectonic plates reveal a compelling correlation. In particular, geoid depressions have been associated with subduction processes occurring in the Mesozoic and Cenozoic[7,14]. Additionally, Spasojevic et al.[4] observed that long-wavelength geoid minima correspond to subducted tectonic slabs in the lower(most) mantle, while positively buoyant mantle above depths of 1000 km is linked to shorter-scale geoid lows, exemplifi d by the case of Antarctica.

These tomography-based models of present-day mantle convection do not establish a direct connection between the past dynamical evolution of the mantle and present-day geodynamic observables. To bridge this gap, we present a comprehensive examination of the time-dependent evolution of Earth's nonhydrostatic geoid,

specifi ally focussing on the complex interaction between slab subduction and hot mantle upwellings that explain the origin of the Earth's largest geoid depression: the Antarctic geoid low (AGL). We further validate the predicted temporal evolution of the AGL by comparing the corresponding time-dependent shifts in Earth's rotation axis – True Polar Wander (TPW) – with independent paleomagnetic constraints. As demonstrated below, it is the time-dependent contribution of an active, anomalously hot, buoyant mantle upwelling centred below the Ross Embayment that is key to understanding the temporal evolution of the AGL.

Methodology: Conceptual framework for mantle convection modelling of geoid anomalies

To test hypotheses regarding the formation of the Earth's strongest geoid low above Antarctica, we employ a robust back-and-forth nudging (BFN) technique that involves a quasi-reversibility (QRV) method for reconstructing the geological evolution of mantle convection[15]. Th s 3D convection model in spherical geometry employs a pseudo-spectral methodology with spherical harmonic basis functions to solve the governing equations for the global conservation of mass, momentum, and energy in a compressible, self-gravitating mantle[16]. Details of forward and time-reversed convection modelling are presented in the Materials and Methods.

We adopt a plate-like mechanical boundary condition at the surface to link lithospheric plate-like motions with underlying mantle fl w. In this framework, surface velocities are not prescribed but emerge through viscous coupling to the buoyancy-driven convective fl w beneath. Th s coupling is guided by the geologically reconstructed evolution of plate geometries over the Cenozoic, derived from seafl or age and paleomagnetic data[17]. It ensures that poloidal (convergent and divergent) and toroidal (strike-slip) components of mantle fl w are dynamically consistent with surface tectonics[18].

Our BFN method for time-reversed convection modelling also incorporates depth variations in mantle viscosity constrained by a wide range of geodynamic observations. Th s input is crucial for ensuring that mantle buoyancy evolves on time scales consistent with Earth's dynamics. Specifi ally, our convection modelling incorporates a depth-dependent, horizontally averaged viscosity derived from joint inversions of the global convection-related observables that include plate velocities, gravity anomalies, crust-corrected dynamic topography, and core-mantle boundary ellipticity. Additionally, this mantle viscosity profile integrates a suite of ice-age geodynamic data associated with glacial isostatic adjustment, notably, the Fennoscandian relaxation spectrum and decay times determined from the postglacial sea level history in Hudson Bay and Sweden[19,20].

As illustrated in Glišović & Forte[15,21,22], seismic tomography models retain a record of past mantle structure, whose evolution – including both upwellings and downwellings – can be reconstructed from the present day into the geological past using suitably formulated time-reversed convection modelling. We employ density anomalies from the GyPSuM tomography model[23] as the initial condition for reconstructing past mantle fl w. Unlike traditional models based solely on seismic data, GyPSuM incorporates a joint inversion of seismic, geodynamic, and mineral physics constraints, ensuring that the resulting 3D density anomalies yield a mantle buoyancy distribution consistent with key seismic and global surface geodynamic observations (free-air gravity anomalies, dynamic topography, tectonic plate motions, and excess core-mantle boundary (CMB) ellipticity, Forte et al.[24]. Th s physical consistency is matched by strong quantitative fits, where GyPSuM achieves a 93% variance reduction fit to global S-wave velocity data, confi ming its agreement with observed seismic structure[23], and where geoid anomalies computed from these density anomalies yield variance reductions of 91% and 85% when evaluated using two alternative viscosity profiles introduced below (V1 and V2, respectively).

Nonhydrostatic geoid anomalies are predicted by spatially convolving mantle density anomalies with geoid kernel functions computed in spherical harmonic space[24,25], and Section "4" in Supplementary Material). These kernels based on the impulse response of a compressible, self-gravitating, viscous mantle derive from viscous-fl w Green functions. According to the plate-coupled mantle-fl w theory[18], this approach requires decomposing internal density anomalies into two components, each convolved with kernel functions appropriate for either a free-slip or no-slip surface boundary condition. The weighting between these boundary conditions depends on the spatial geometry of tectonic plates and enforces kinematic consistency between surface plate motions and internal mantle fl w.

To assess model robustness and characterize uncertainty, we conducted sensitivity analyses focused on the influence of key inputs – mantle viscosity profiles, plate velocity reconstructions, and seismic tomography models – on predicted geoid evolution. These tests, detailed in Supplementary Material (Sections "2" – "3"), show that while amplitude and timing of geoid anomalies may vary across different model realizations, the emergence and persistence of the AGL are robust, with consistent timing of its major transition across all tested model configur tions.

The importance of testing a range of candidate viscosity and tomography models has been acknowledged in prior studies, such as Liu & Zhong[26], who examined present-day geoid compatibility using instantaneous fl w simulations. Similar efforts, including Liu & King[27], have primarily targeted reproducing the present-day geoid, yielding at best a static view of mantle conditions. These approaches, however, did not account for time-dependent evolution of mantle structure. Unlike these studies, our modelling reconstructs the full Cenozoic evolution of geoid anomalies using time-reversed convection, incorporating multiple viscosity and tomography models, along with independent observational constraints such as TPW.

A detailed validation of the temporal evolution of the degree-2 component of our predicted geoid fi lds, using independent paleomagnetic data, is presented in the Supplementary Material (Sections "4" – "5"). Reproducing the correct evolution of the degree-2 component of the global geoid anomalies is critical for understanding deep mantle structure and for constraining the long-term stability of Earth's rotation. Comparisons with paleomagnetic data (notably Table S2) show that our models can also reliably capture the essence and timing of TPW events over the past 70 Myr, further validating the time-dependent mantle fl w reconstructions. Agreement with TPW observations provides a stringent benchmark that reinforces confide ce in the model's higher-degree ($\ell > 2$)

geoid structure, although it does not by itself guarantee fid lity at those higher degrees (Sections 6 and 7 of the Supplementary Material). Th s validation applies explicitly to the past time-evolving degree-2 geoid structure, while confide ce in the full spectral range is further supported by the <2% BFN round-trip mismatch (Fig. S10) and by the high variance-reduction fits to the present-day geoid (~93% for tomography-based initial models and ~85% for the observed anomalies, Table S1).

Results: Evolution of the AGL driven by coupling between positive and negative buoyancy

Predicted time-dependent geoid anomalies show that a prominent geoid depression at the present-day AGL position has persisted for at least 70 million years (Fig. 2). However, the locus of the maximum global geoid depression was centred over the South Atlantic Ocean between 30°S and 45°S at the beginning of the Cenozoic (Fig. 2A). Th s depression subsequently underwent a rapid spatial shift to the Ross Embayment between 40 and 30 Ma (Fig. 3), accompanied by a substantial increase in amplitude of the associated geoid low (Figs 2B & C).

Analysis of the geoid low's temporal evolution at the present-day AGL position reveals two distinct phases (blue curve in Fig. 4A): from 70 Ma to 35 Ma, when the amplitude fluctuated (fi st strengthened and then weakened), and from 35 Ma to the present, during which it increased by 30%. The sensitivity and uncertainty analyses presented in the Supplementary Material (Section "2") show that all convection models considered, employing different tomography and viscosity models, concur that the time window from 50 to 30 Ma marks a robust transition in the evolution of the AGL (see Fig. S2b), while the precise amplitude trajectories vary across models. In contrast, the temporal evolution of the maximum global geoid low whose position varies spatially (Fig. 3) undergoes a small reduction between 70 Ma to 50 Ma, followed by a decrease from 50 to 35 Ma, and a subsequent increase in amplitude over the last 30 million years (red curve in Fig. 4A). In almost all cases, we fi d a small reduction in amplitude of the AGL over the last 5 million years (Fig. S2a).

We also tested the predicted AGL evolution against paleomagnetic constraints on TPW, which depend on the time-dependent degree-2 geoid (Section "4" of Supplementary Material). In the Supplementary Material (Section 5 and Fig. S3), we demonstrate that these paleomagnetic-based TPW paths exhibit a pronounced shift in trajectory – resembling a hairpin- or U-turn – at approximately 50 Ma that is matched by the TPW predicted by the mantle convection models. Th s shift closely aligns with the key transition in the AGL's evolution identifi d in our mantle fl w reconstructions (Fig. S2b). The agreement between the modeled geoid changes and the independently inferred TPW variations provides a critical calibration, confi ming that our predicted degree-2 geoid evolution is consistent with global rotational dynamics constrained by completely independent paleomagnetic observations.

Mantle convection reconstruction during the Cenozoic show that the relatively stable evolution of the geoid depression at the present-day AGL position can be largely attributed to quasi-static evolution of density anomalies within the lower half of the mantle (Fig. 4B). A ~1000 km-thick layer in the lowermost mantle contributes ~30% of the total geoid amplitude at the beginning of the Cenozoic Era, reaching a peak contribution of ~50% between ~40 and ~5 Ma (Fig. 4C). Additionally, a strong decrease in the amplitude of the geoid contribution provided by mantle buoyancy in the layer between ~500 and ~1300 km depth is primarily responsible for the fluctuation in the AGL between 70 and 35 Ma. A key fi ding concerns the origin of the rapid strengthening of the geoid low amplitude that began at 35 Ma (Fig. 4B). Prior to this time, the mid-lower mantle (between ~1300 and ~1800 km depth) provided a stable contribution to the geoid depression at the AGL location. However, between 35 Ma to the present, this mid-mantle contribution signifi antly decreased, surpassed by the steadily increasing contribution of density anomalies from depths shallower than ~1300 km (Fig. 4B). The gradual growth of this upper mantle contribution, accompanied by the corresponding decline of the mid-mantle contribution, drove the substantial amplifi ation of the AGL's magnitude over the past 35 million years. The origin of this shift toward contributions from shallower mantle depths, where the buoyancy contribution accounts for ~40% of the AGL's present-day amplitude, is elucidated in the following discussion.

At 65 Ma, the A1-A2 cross-section (Fig. 5A) reveals a prominent deep-mantle downwelling system extending from the southern Atlantic sector near the present-day Scotia subduction zone (21°W,54°S) to Coats Land (18°W,78°S). A coherent high-density anomaly is observed in the upper mantle beneath the southern Weddell embayment, dipping northward from Coats Land. Simultaneously, a second slab-like structure dips southward toward this same region from the vicinity of the Scotia subduction zone, reinforcing the interpretation of a dual-sided convergence geometry across the Weddell sector.

Th s downwelling system, together with a second slab-like anomaly located north of Australia, ultimately converges in the lowermost mantle, above the core-mantle boundary, beneath a broad, positively buoyant lower-mantle upwelling centred beneath the present-day AGL (cross-sections A1-A2 & B1-B2 in Fig. 5A). The lateral extent of this upwelling reaches toward the Australian margin (C1-C2), forming a dome-like structure flanked by two long-lived downwelling systems. By 40 Ma, the core of this mantle upwelling – identifi d by the strongest low-density anomalies – continues its ascent through the lower mantle, approaching the upper mantle (Fig. 5B). At the long wavelengths relevant here, the gravity kernels (Fig. S11c, d) place positive weights on density anomalies between ~300 and ~1300 km depth; thus, the upwelling's negative density contributes to amplifying the negative geoid low at the surface. Although the upwelling's dynamic-topography uplift contributes positively to the geoid, this term is smaller at these wavelengths and does not off et the direct contribution from the internal mass term; the net effect is a stronger geoid low as the anomaly rises beneath the AGL (Fig. 5B, C). Over the subsequent 40 million years, the anomaly rises further beneath the AGL (Fig. 5C), consistent with the progressive vertical ascent of buoyant material over time. Th s long-lived upwelling structure is a principal source of the present-day negative geoid anomaly, and its temporal evolution directly underpins the trends shown in Fig. 4.

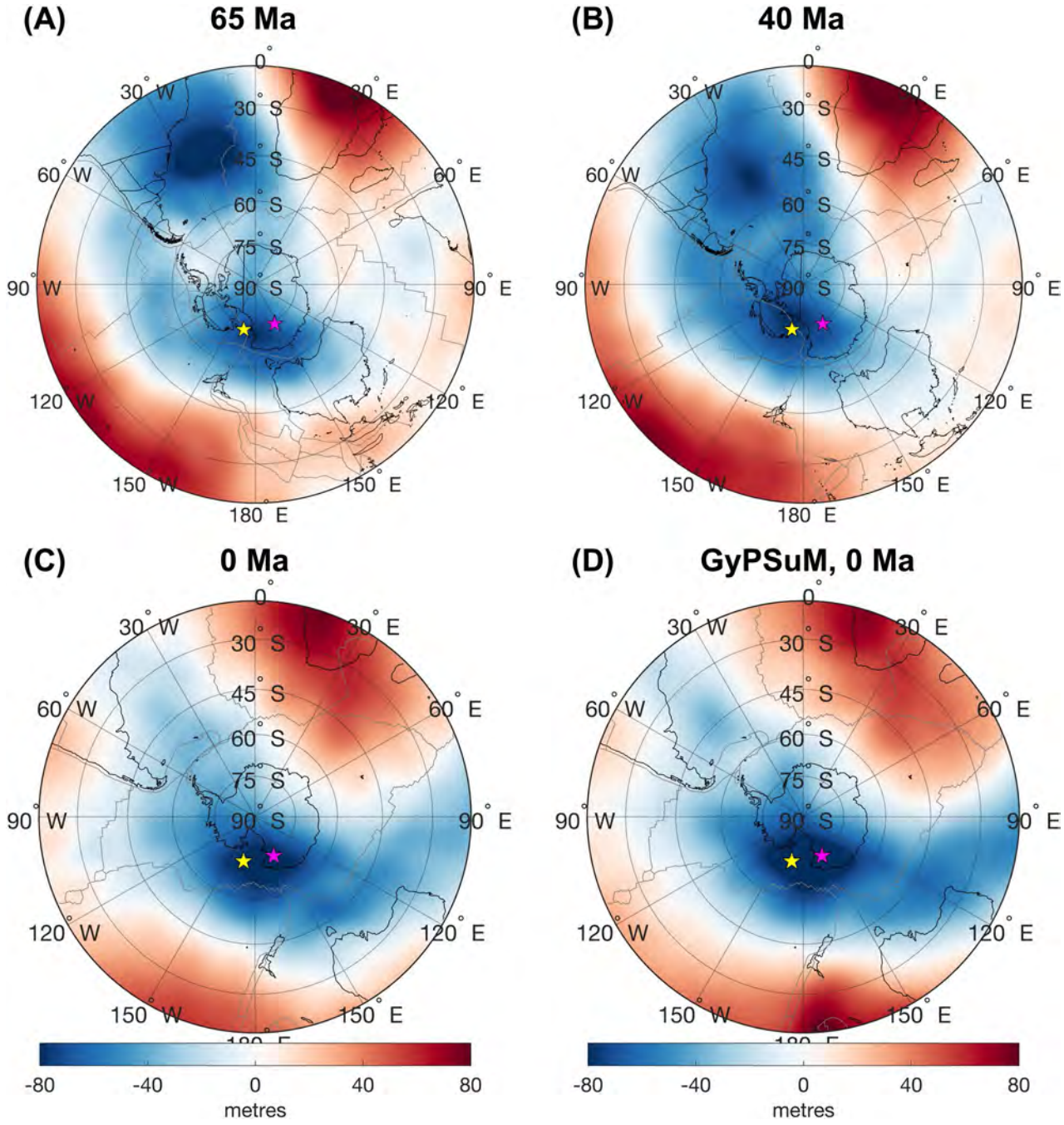

Fig. 2. Time-dependent geoid predictions. Geoid anomalies are shown at: (**A**) 65 Ma, (**B**) 40 Ma, and (**C**) 0 Ma, predicted from the time-dependent reconstruction of 3D mantle structure at 70 Ma. (**D**) The geoid anomalies based on present-day GyPSuM tomography model[23]. In all cases, the V1 viscosity model[20] is employed, and the geoid predictions are represented by a spherical harmonic expansion truncated at degree 32. The yellow star marks the present-day geographical location of Earth's lowest point for nonhydrostatic geoid based on the Chambat et al.[6] ellipticity correction. The magenta star marks the location of the maximum geoid depression after removal of the gravitational signal generated by isostatically compensated crustal heterogeneity[20]. Th s crust-corrected, nonhydrostatic geoid was employed as a constraint in the derivation of the GyPSuM tomography model. The black and grey lines display the reconstruction position of the plate boundaries and coastlines[28]. Regional variance reduction values over Antarctica (lat ≤ –60°) are: 94 % (observation, Fig. 1B, vs. initial GyPSuM model, Fig. 2D),88 % (observation, Fig. 1B, vs. prediction, Fig. 2C),and 96 % (initial GyPSuM model, Fig. 2D, vs. prediction, Fig. 2C).

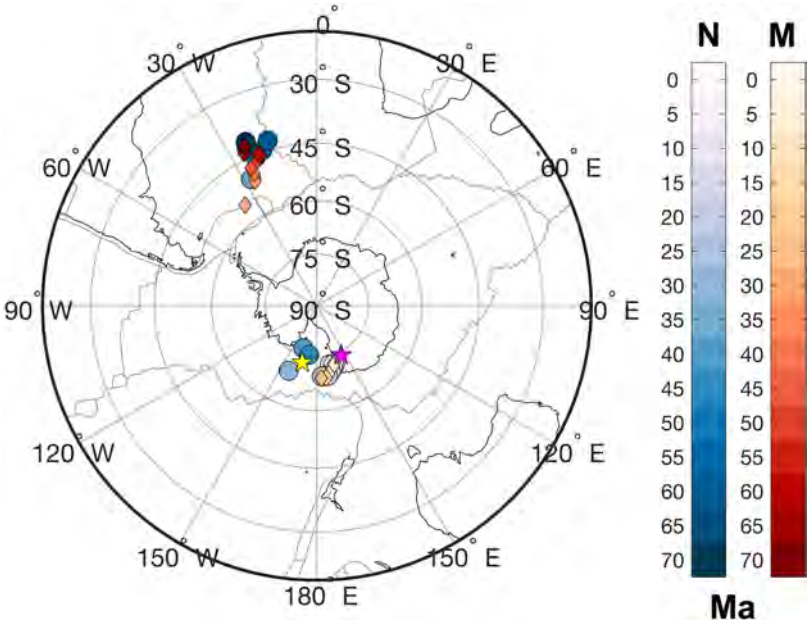

Fig. 3. The time-dependent variations in the predicted geographical location of Earth's lowest geoid point. The blue shaded circles represent the geoid predictions obtained with time-dependent mantle convection models that do not enforce a match to the geologic estimates of past plate motions (N). The red shaded diamonds represent the geoid predictions obtained with convection models whose internal buoyancy is nudged to yield an exact match to the past plate motions (M). The colour gradation ranges from the lighter hues (the lightest one represents 0 Ma) to deeper tones (the deepest one represents 70 Ma). As in Fig. 2, the stars mark the present-day location of Earth's maximum nonhydrostatic geoid depression based on the[6] ellipticity correction (yellow star) and after removal of the gravitational signal of isostatically compensated crust (magenta star). The black and grey lines display the present-day position of the plate boundaries and coastlines.

Discussion and conclusions

Our mantle reconstructions reveal that the density anomalies in the lower 1000 km of the mantle provide a long-term, stable contribution to the AGL of about ~30–50% of its total amplitude. In contrast, upper-mantle layers above ~1300 km depth show greater temporal variability, becoming increasingly signifi ant over the past 35 million years (Fig. 4).

These fi dings are buttressed by the geodynamic consistency of our mantle reconstruction methodology, most notably by its ability to return to the present-day geoid and to match this key observable with high fid lity. Specifi ally, after reconstructing mantle structure backward in time to 70 Ma using the BFN technique, we simulate forward mantle convection and recompute present-day geoid anomalies. These V1-forward predictions yield variance reductions of 85–87% relative to the observed geoid, and 93–94% relative to the initial GyPSuM-predicted geoid anomalies (Table S1). Th s round-trip agreement confi ms that our modelling approach not only recovers present-day observables but also preserves the essential features of the initial internal buoyancy structure – demonstrating dynamic consistency and numerical stability over a 70 Myr double-integration loop. Since geoid anomalies presented here are truncated at spherical harmonic degree $\ell = 32$, our model results incorporate the robust evolution of predicted mantle density structures across those spatial scales.

The robustness of the BFN algorithm is further demonstrated in Fig. S10, which presents the variance reduction between backward-in-time reconstructions and forward-in-time predictions of the full 3-D temperature fi ld, evaluated at 2.5 Myr intervals over the past 70 million years. These reconstructions, initialized with the GyPSuM model and V1 viscosity profile, span spherical harmonic degrees up to $\ell = 170$ and all 129 radial Chebyshev levels. In each time interval, the reconstruction-to-prediction mismatch remains below 2%, with variance reduction values consistently exceeding 98%. The total temporal accumulation of mismatch across all time windows is ~24%, highlighting the method's ability to tightly constrain numerical error propagation throughout the full integration interval. In the context of inverse problem theory, this cumulative error provides an estimate of uncertainty for the entire spectral range up to $\ell = 170$. Consequently, the uncertainty in our long-wavelength geoid anomalies (corresponding to $\ell \leq 32$) must be smaller, consistent with our ~4–6% geoid prediction error (Table S1). These considerations further underline the fid lity of the reconstructed mantle structure and the predictive reliability of the BFN framework from 70 Ma to the present. We also include a time-dependent degree-2 benchmark: the model-predicted $\ell = 2$ geoid evolution is compared to TPW over the past 70 Myr, with goodness-of-fit values summarized in Table S2 (using the reduced-$\chi 2$ metric defi ed in the Supplementary Material), providing a necessary constraint on the time-varying low-degree signal.

A key concern in evaluating the geologic realism of these mantle convection reconstructions is the issue of 'ground truthing'. Further validation of the temporal evolution of these mantle reconstructions was provided by past work that linked deep mantle upwellings to major volcanic events, such as the formation of Deccan Traps,

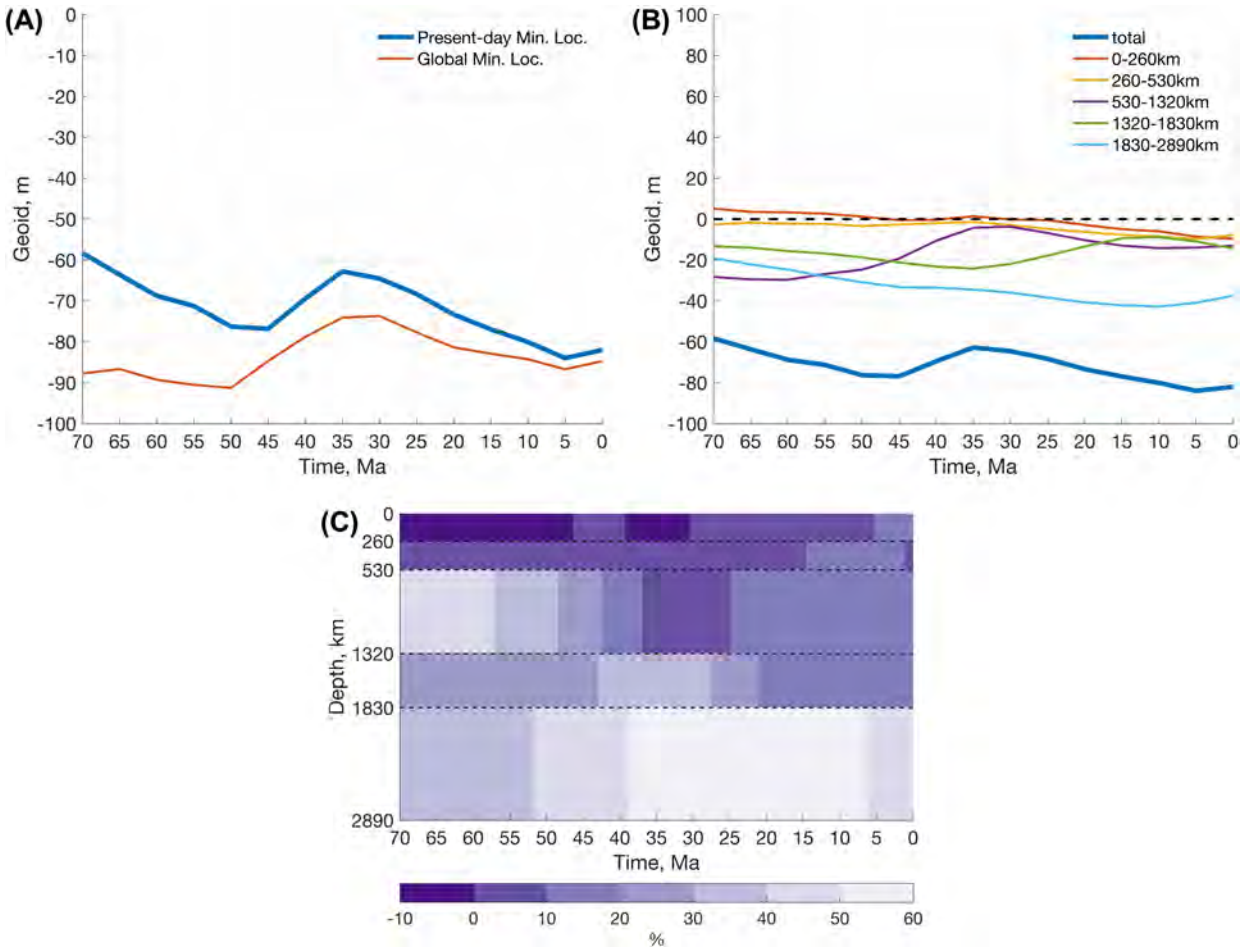

Fig. 4. Time-dependent mantle contributions to the Antarctic Geoid Low (AGL). (**A**) The red line depicts the temporal changes in the geoid anomaly above the spatially shifting locations of the global geoid minimum, while the blue line represents the geoid anomaly above the present-day location of the AGL. (**B**-**C**) Per-layer density anomaly contributions to the AGL. (**B**) The total geoid anomaly (Gt) is illustrated by the dark blue line, accompanied by per-layer contributions indicated by additional lines (Note: Gt = G0-260 + G260-530 + G530-1320 + G1320-1830 + G1830-2890). (**C**) The per-cent layer contributions are presented relative to the total geoid.

providing a robust example of how these models reveal the interplay between deep mantle sources and surface geology[21]. Additionally, spatio-temporal connections between deep mantle processes and surface geological features, such as the Nile River drainage basin and the North Atlantic Igneous Province, were established, offering concrete evidence to support these models[22,29]. Together, these ground truthing efforts underscore the reliability of our 4-D reconstructions, providing a solid foundation for understanding the complex interactions between deep mantle dynamics and surface geological phenomena.

However, in the present study we focus on mantle dynamics in the Southern Hemisphere, particularly the Antarctic region. In the following, we therefore evaluate our reconstructions by comparing modelled mantle structures to prominent tectonomagmatic features that fall directly along the great-circle cross-sections A1–A2, B1–B2, and C1–C2 (Fig. 5), where dynamic mantle processes intersect well-documented surface geological phenomena. These comparisons offer spatially and temporally consistent observations that reinforce the geologic plausibility of our reconstructions and substantiate our fi dings concerning the dynamic origin of the AGL.

The reconstructed Cenozoic fl w patterns reveal large-scale downwellings of high-density material extending from the southern Atlantic sector near the present-day Scotia subduction zone to the Weddell Sea margin adjacent to Coats Land at 65 Ma (Fig. 5A). Although mantle structure prior to 65 Ma was not reconstructed, the persistence of deep subduction suggests long-lived descent of slab material operating throughout the Mesozoic. Concurrently, an upwelling situated beneath the present-day location of the AGL has been actively transporting hot, low-density material from the lowermost mantle to the Earth's surface. Over time, the vigour of this sub-Antarctic convective fl w has diminished, yielding a present-day mantle structure characterized by a deep repository of subducted material and persistent low-density anomalies in the mid-to-upper mantle (Fig. S9).

To further substantiate the reconstructed large-scale downwellings, we compare their spatial extent and morphology with combined tectonic-tomographic interpretations of slab anomalies beneath the Scotia and Weddell regions[30]. Specifi ally, a high-density anomaly associated with the present-day Scotia subduction zone,

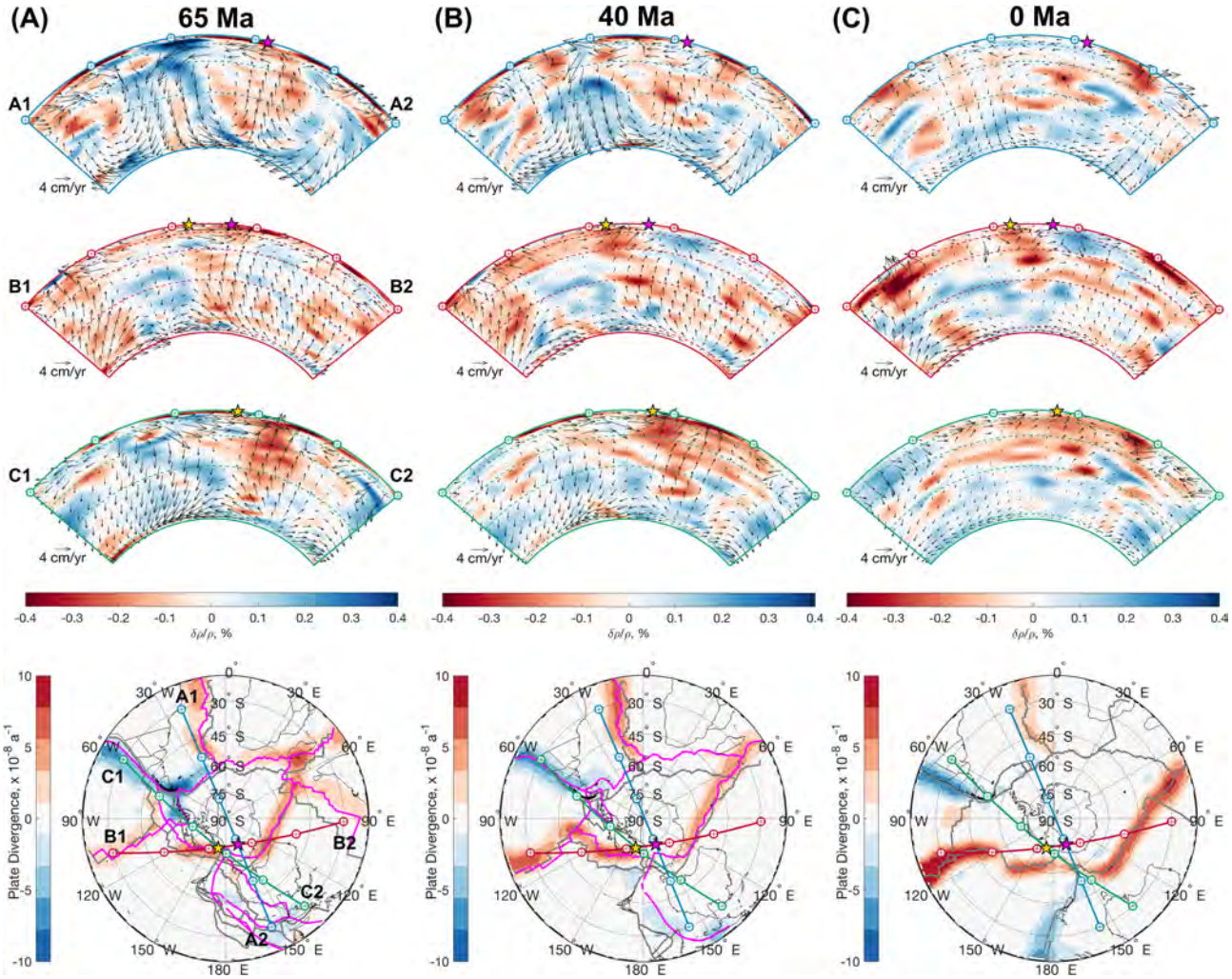

Fig. 5. Convection reconstructions of mantle heterogeneity beneath Antarctica at three times. (**A–C**) Great-circle cross sections along the minor arcs A1–A2 (blue), B1–B2 (red) and C1–C2 (green) show lateral density anomalies, δρ/ρ (%), whose evolution is predicted by a reconstruction of mantle convection initialized with the GyPSuM tomography model[23] and using the V1 radial viscosity profile[20]. The forward-in-time reconstruction, beginning at 70 Ma, is shown at three different instants: (**A**) 65 Ma, (**B**) 40 Ma, and **(C)** 0 Ma. The sections extend from the surface to the core–mantle boundary (2,890 km). Dashed horizontal lines mark 220 km, 660 km, and the mid-mantle horizon at 1500 km. Black arrows are instantaneous velocity vectors in the section,the scale bar corresponds to 4 cm yr^{-1}. The mantle evolution shown here is from the N-V1 simulation, in which there is no explicit assimilation of geological estimates of past plate velocities. Bottom row: South-polar stereographic maps indicate the locations and orientations of the section arcs (A1–A2, B1–B2, C1–C2) and show the model-predicted plate-divergence fi ld (units:10^{-8} a^{-1}) computed from the instantaneous surface velocity derived from the internal buoyancy at each epoch (spherical-harmonic truncation ℓ = 32). Reconstructed plate boundaries and coastlines from Merdith et al.[28] are plotted in black/grey, plate boundaries from Rowley et al.[17], fi ed Indo-Atlantic hotspot frame, in magenta. The yellow and magenta stars indicate the present-day location of the deepest nonhydrostatic geoid minimum as defi ed in Fig. 2. Consistent with the Rowley et al.[17] plate reconstruction (magenta lines), the 65 Ma plate-divergence predicted by the N-V1 model (bottom left ap) exhibits a continuous negative-divergence (convergence) belt along the South Pacific argin that branches to the Antarctic Peninsula and the South Scotia Sea.

with a midpoint surface projection at 32°W, 56°S, aligns well with our reconstruction at 21°W, 54°S. A separate anomaly, the South Orkney Island slab, is imaged in the mid-mantle beneath Coats Land and the southern Weddell sector, trending NW-SE and interpreted as paleo-Pacific lithosphere subducted at the Gondwana margin, with rollback and subduction terminating by ~94 Ma. Additionally, a deeper anomaly – the Georgia Islands slab – is identifi d at the core-mantle boundary and interpreted as a remnant of Late Palaeozoic to Early Mesozoic subduction, with inferred slab detachment between 200-180 Ma. The spatial coincidence and depth separation of these three anomalies suggest a transient slab regime along this corridor, characterized by successive phase of subduction and slab detachment events over a span of more than 250 million years. Although the deeper portions of the Scotia anomaly are poorly resolved, as acknowledged by van der Meer et al.[30], the

tomographic evidence provides critical, independent support for the longevity, structure, and dual-sided nature of the downwelling system inferred in our reconstructions.

Beyond tomographic interpretations, additional independent evidence further corroborates our reconstruction. Riley et al.[31] document Late Cretaceous-Paleogene calc-alkaline and intra-oceanic arc magmatism along the South Scotia Ridge, providing direct geological evidence consistent with the subduction system we reconstruct at 65 Ma (Fig. 5A). In addition, numerical experiments by Schellart et al.[32] simulating westward-directed subduction initiation in the Scotia region yield slab geometries strikingly similar to the dual-sided convergence pattern (cf. our Fig. 5A with their Fig. 8). Together, these complementary geological and geodynamic studies provide convergent evidence supporting the existence of a South Atlantic subduction system extending from Coats Land to the Scotia Sea in our backward-in-time-mantle fl w reconstructions.

While these independent studies strengthen the geological plausibility of our reconstructions, it is equally important to recognize the methodological limitations of static tomographic age determinations. Critically, van der Meer et al.[30] estimate subduction ages without employing dynamic modeling of slab sinking, relying instead on depth-to-age correlations guided by stratigraphic, metamorphic, and plate kinematic records. As they emphasize, "detached lower mantle slabs may be associated with a large number of geological records, since post-detachment plate motions may have displaced these records over thousands of kilometres." Th s intrinsic limitation underscores the value of dynamically consistent, backward-in-time reconstructions such as those presented here, which resolve both the spatial origin and temporal evolution of the subducted slabs. As further highlighted by Rowley[33], more than 50% of the oceanic lithosphere younger than 55 Ma has already been subducted, necessitating extrapolation in global plate reconstructions. Our reconstructions thus offer critical, dynamically constrained insights into slab evolution in regions where conventional plate kinematics and seismic imaging alone face fundamental limitations. As shown in Fig. 5A (bottom left), the model-predicted plate-divergence fi ld at 65 Ma exhibits a continuous negative-divergence (convergence) belt along the South Pacific margin that branches along the Antarctic Peninsula and the southern margin of the Scotia Sea – consistent with the subduction implied by the plate reconstructions in Rowley et al.[17] and other tectonic reconstructions[28]. Th s predicted pattern of convergence comes from the buoyancy-driven Stokes-fl w solution in the N-V1 model, in which there is no assimilation of geological estimates of surface plate velocities (see Materials and Methods).

In addition to the downwelling system, our reconstructions resolve a broad, thermally driven upwelling beneath the present-day AGL and its surrounding region. While the presence of low-density anomalies in the mid-to-upper mantle (as revealed in Fig. S9) is consistent with fi dings of Spasojevic et al.[4], our temporal reconstructions reveal a distinct dynamic setting for the AGL. The instantaneous fl w models of Spasojevic et al.[4] led these authors to propose that upwelling in the mid-to-upper mantle is caused by hydration-induced buoyancy generated through processes above subducted slabs. By contrast, our reconstructions show that low-density material in the mid-to-upper mantle originates from the lowermost mantle. Moreover, the mineral physical relations incorporated in the joint tomography inversions carried out by[23] reveal that the positive buoyancy in the deep-seated mantle upwelling below the AGL is consistent with a thermal origin. Lagrangian tracking of passive tracers[22] reveals that particle trajectories in the mantle upwelling below the AGL originate from the seismic D" layer at the bottom of the mantle (Fig. S9). The transit times associated with these particle trajectories suggest that the upward transport of hot mantle material by this upwelling has been active for the entirety of the Cenozoic era (Fig. 5A) and extends well back into the Mesozoic era. In sum, our inference is one of thermal suffici cy – the upwelling plumes we model below Antarctica are consistent with a classic thermally-driven source – but cannot formally exclude hydration effects. The explicit convective modelling of volatile transport is a target for future model extensions.

To contextualize the reconstructed upwelling beneath the AGL, in the following we examine its evolution within the broader tectonic and mantle convective framework of the southern polar region. Th s allows us to assess how large-scale mantle processes may have interacted with lithospheric dynamics and contributed to the present-day structure and elevation of East Antarctica.

As discussed above, our reconstructions of mantle convection (Fig. 5) suggest that mantle upwellings beneath the AGL originate from deep sources within the seismic D" layer (Fig. S9). Th s fi ding aligns with the interpretations of Bredow et al.[34], who emphasize thermal anomalies beneath Marie Byrd Land and Ross Island as potential indicators of mantle upwelling. Their fi dings suggest these anomalies may arise from tilted plume conduits or subduction-driven mantle fl w rather than classical deep mantle plumes. While Bredow et al.[34] are cautious about the existence of a mantle plume beneath West Antarctica, our modeled particle trajectories in Fig. S9 indicate the sustained ascent of buoyant material from the lower mantle. Th s evidence complements their observations of elevated dynamic topography, particularly beneath West Antarctica, which may result from a combination of shallow lithospheric thinning and deeper thermochemical anomalies.

The reconstructed upwellings below West Antarctica (Figs. 5 & S9), also align with interpretations by Panter[35], who considered the interplay between mantle plumes, edge-driven fl w, and metasomatized lithosphere as sources for magmatism in the West Antarctic Rift System. The buoyant ascent of deep mantle material in our models supports the hypothesis that HIMU-like geochemical signatures beneath Marie Byrd Land and the Ross Sea may originate from ancient subduction-modifi d sources, as proposed by Panter[35]. Furthermore, our fi dings suggest that these large-scale deep upwellings may interact dynamically with lithospheric thinning and, potentially, with shallow small-scale edge-driven fl w, processes that are theorized to have occurred during the Eocene[35].

The ascending mantle upwelling beneath the AGL, reconstructed in our models from 65 Ma onward, provides an independently derived, dynamically consistent mechanism for broad and sustained uplift beneath central East Antarctica. Th s feature is spatially coincident with the present-day Gamburtsev Subglacial Mountains and aligns in timing with rift reactivation and thermal support phases proposed by Ferraccioli et al.[36]. Their interpretation of a long-lived uplift phase following Cretaceous rifting is consistent with the progressive rise

of low-density mantle material inferred in our reconstructions. In contrast to models requiring lithospheric thinning or delamination, our results suggest that a coherent, deep-mantle buoyant anomaly – whose ascent may have been triggered by ancient (Mesozoic) downwelling slabs – may have played a fundamental role in supporting the high topography of interior East Antarctica, including the nucleation region of the East Antarctic Ice Sheet.

During the time interval ~58–50 Ma, Williams et al.[37] document the final stages of Australian-Antarctic breakup, with separation in the South Tasman Rise region and acceleration of seafloor spreading along the Southeast Indian Ridge. This tectonic transition coincides with mantle processes, particularly the ascent of a hot buoyant upwelling that we identify as dominant contributors to the recent development of the AGL. Notably, these processes involve rapid thinning of the lithosphere and dynamic upper mantle flow associated with the Wilkes Land margin and adjacent oceanic crust. Our mantle flow reconstructions (Figs 5A & B) suggest that these younger contributions from the upper mantle are superimposed on the longer-term density anomalies that evolved in the deep mantle during the earlier Cretaceous phases.

The mantle-driven shift in the geoid between ~40 and 30 Ma could contribute to changes in relative sea level (RSL), which is defined as the difference between the ocean equipotential (the geoid) and the solid-Earth surface[38]. On Myr timescales the ocean surface follows the geoid, but the geoid and solid-surface topographic responses are governed by distinct viscous-flow response kernels[10,24] that differ, especially for deep (e.g. mid-mantle) buoyancy sources. As a consequence, geoid and topography fields can diverge, because geoid kernels change sign with depth (Fig. S11c, d) whereas topography kernels do not (Fig. S11e, f). This distinction highlights that mantle-driven geoid shifts need not be mirrored by surface topographic responses. Of particular relevance is their temporal coincidence with the onset of Antarctic glaciation around 34 Ma – a connection we target as a hypothesis for future testing.

Building on this, we hypothesize that RSL changes, arising from the combined evolution of geoid and dynamic topography driven by mantle processes beneath Antarctica could have influenced the boundary conditions relevant to ice nucleation. Prior work emphasizes that sea-level fluctuations driven by both global ice volume changes and regional tectonic/mantle forcing help shape Antarctica subglacial topography[39]. In that context, our results motivate a targeted test of whether long-wavelength RSL anomalies linked to AGL might have been conducive to the growth of Antarctic ice sheets. Modeling these effects is beyond the scope of the present study.

The mechanisms and magnitude of any RSL or climate impacts thus remain speculative at this stage. A quantitative assessment will require coupling our time-dependent geoid to modeled dynamic topography and solving the self-gravitation/sea-level problem[38] with an Earth rheology consistent with our flow models[40], followed by comparison with independent geological proxies[39]. We defer this analysis to future work that also focusses on controlling uncertainties in reconstructing past topography and sea level changes, as highlighted by Paxman et al.[39]

Materials and methods

To solve the direct (forward-in-time) problem of thermal convection in the Earth's mantle, we use the system of governing equations that satisfy conservation of mass, momentum, and energy for a Newtonian viscous fluid in a compressible and self-gravitating mantle[16]. Details concerning the solution of the regularized, time-reversed energy equation are presented in Glišović & Forte[41].

We carry out all flow computations using spherical harmonic expansions up to a maximum harmonic degree of 170, which yields a horizontal spatial resolution that varies from ~64 km at the core-mantle boundary to ~117 km at the top of the mantle. The vertical resolution is defined with a Chebyshev polynomial expansion up to order 129 which yields a radial-resolution length scale ranging from ~0.4 km near the (upper and lower) boundaries to ~35 km in the middle of the mantle.

The reference structure (density, gravity, thermal conductivity, heat capacity, thermal expansion, and internal heating) follows Glišović & Forte[22].

The single most critical input for the mantle convection simulations is the 3-D distribution of lateral density (and corresponding temperature) anomalies derived from the GyPSuM global tomography model[23]. Global checkerboard-style resolution tests that cover the Southern Hemisphere and hence Antarctica, were carried out for the seismic shear-wave data employed in the derivation of the GyPSuM model[42]. These tests quantify both pattern recovery or cross-correlation (CC) and amplitude recovery (AR) by depth. The resolution tests employing 5° checkerboards (see Appendix B in Simmons[42]), yield CC = 0.59–0.90 (CC ≥ ~0.70 for most layers, for the "rough" inversion) and AR = 53–87% (AR ≥ ~70% for most layers, for the "rough" inversion). The weakest recovery that is identified is in the Southern Hemisphere oceans in the depth range: 175–525 km.

GyPSuM uniquely integrates seismic and geodynamic data with mineral physical constraints, ensuring that the inferred buoyancy field is consistent with key geophysical observables. In our models, we use the total density anomalies from GyPSuM, which were optimized in the joint inversion to provide the best simultaneous fit to seismic and geodynamic observations. The $\delta\rho$ in GyPSuM comprise thermal anomalies plus a non-thermal (residual) component admitted by the joint inversion to reconcile seismic and geodynamic data. Non-thermal is here defined as the portion of density not captured by 1.5-D mineral physics scaling employed in GyPSuM[23], it can include true compositional effects and unmodelled physics such as laterally varying anelasticity (seismic Q) that modifies the local δV_S–temperature relation, as well as other scaling and resolution limitations. One such limitation (or un-modelled effect) is the neglect of topography on the 410 and 660 km seismic discontinuities. Glišović et al.[43] demonstrate that when discontinuity topography is explicitly modelled in the joint seismic-geodynamic inversions, the non-thermal density amplitudes in the mid- and deep-mantle are significantly reduced.

For completeness, we also considered the S40RTS global tomography model[44] to assess uncertainties associated with density model choice (see below and Supplementary Material: Sections "2" & "3"). Unlike GyPSuM, which

jointly describes relative perturbations in P-velocity, S-velocity, and density throughout the mantle, the S40RTS model is derived solely from seismic S-velocity data. Therefore, S40RTS requires an a-posteriori conversion to density. For S40RTS, we use a $\delta\rho$–δV_S relation, $R_{\rho/S}(r)$, that is optimized for any assumed mantle viscosity profile (e.g. V1 or V2) via an Occam-style inversion of the surface geodynamic observables[24]. It is conceivable that allowing a fully 3-D scaling ratio, $R_{\rho/S}$, which is inherent in the joint inversions for GyPSuM, could further improve S40RTS fits to the global geodynamic observables, but such an iterative and nonlinear inversion is beyond the scope of this paper.

We then defi e an effective temperature anomaly, δT_{eff}, through: $\delta\rho = -\rho_0(r)\,\alpha(r)\,\delta T_{eff}$, where $\rho_0(r)$ and $\alpha(r)$ are the reference density and thermal expansivity profiles. δT_{eff} is used solely as a computational carrier of total buoyancy in the coupled advection–diffusion and Stokes system; where residual (non-thermal) density exists, it must not be interpreted as an exact thermal fi ld. The same $\rho_0(r)$ and $\alpha(r)$ are used to compute δT_{eff} for both GyPSuM and S40RTS, ensuring a consistent buoyancy–temperature mapping for the dynamics. δT_{eff} is a computational proxy that carries the total buoyancy through the energy equation. (We reiterate that in regions containing non-thermal residuals it should not be interpreted literally as a thermal perturbation.) Two factors limit the concern that this treatment would "diffuse chemistry": (1) with mantle diffusivity $\kappa \approx 10^{-6}\,m^2\,s^{-1}$, the diffusive length scale $\sqrt{\kappa t}$ is ~50 km (corresponding to harmonic degree ℓ=*400*) over 70 Myr – well below the tomography resolved wavelengths – so large-scale, non-thermal buoyancy is not smeared; and (2) our back-and-forth nudging (2.5 Myr windows) constrains spectral drift, keeping the variance misfit to the initial/starting fi ld < 2% per window.

More broadly, we emphasize that joint tomography models such as GyPSuM, through their incorporation of geodynamic constraints and mineral physics priors, in addition to seismic data, provide sensitivity to mantle structure even in regions where seismic coverage is sparse, such as Antarctica. While this approach cannot fully remove regional uncertainties, and may risk local overcompensation, it nevertheless improves the ability to fill gaps where seismic information is limited. Importantly, density anomalies derived from tomography are simultaneously the best available means of initializing mantle convection models and also a source of uncertainty in reconstructing past mantle heterogeneity.

Glišović & Forte[15,41] noted that seismic tomographic resolution of lateral variations in the upper mantle – particularly their amplitudes – is often insuffici t owing to the effects of damping that are inherent in the tomography inversions. The seismically inferred lateral temperature variations are unlikely to be in thermodynamic balance with the strong radial temperature gradients within the thermal boundary layers (TBL) in the lithospheric mantle and above the core-mantle boundary (CMB). Thermodynamic imbalance may introduce signifi ant instability and potential inaccuracies in backward modelling. Consequently, we employed a purely adiabatic geotherm without (upper and bottom) TBLs and thereby minimize these instabilities while ensuring that our models robustly resolve the mantle's large-scale thermal structure, which is essential for accurately reconstructing the mantle's past dynamics. We constructed this adiabatic geotherm based on the mean temperature at the top of the upper mantle transition zone given by Katsura et al.[45], where the temperature at the phase change horizons at 410 km and 660 km depth are 1760 K and 1880 K, respectively. We use isothermal conditions for the surface and the CMB. The surface potential temperature is 1600 K and the resulting adiabatic temperature at the CMB is 2456 K.

As discussed in the main text (see also Supplementary Material – Section "1"), we employ depth-dependent viscosity inferences (Fig. S1) that have been verifi d against a wide suite of geodynamic surface constraints[19,20] and independent mineral-physical modelling[46].

To ensure consistency with past tectonic reconstructions, a key facet of our backward convection modelling involves the incorporation of a plate-like mechanical boundary condition at the top of the mantle[16]. Th s boundary condition, involving the application of geologic reconstructions of tectonic plate geometries, built from paleomagnetic and seafl or age data, and expressed in the Indo-Atlantic hotspot reference frame over the Cenozoic Era[17], explicitly couples the motions of effectively rigid tectonic plates to the underlying mantle fl w. The coupling is implemented in the no-net rotation (NNR) reference frame and dynamically generates both poloidal (divergent and convergent) and toroidal (strike-slip) components of mantle fl w[18], with toroidal motion arising through viscous coupling to the poloidal fl w. Surface plate velocities are not prescribed but emerge through this coupling to the buoyancy-driven mantle fl w at each time step[16]. Geological reconstructions of past plate motions thus serve as direct constraints on the evolution of mantle buoyancy, which we can assimilate into our time-reversed convection models via a formal inverse method that computes the minimal perturbation to the reconstructed 3-D density fi ld required to reproduce these motions. Th s approach enables an objective mapping of mantle regions where only a minimal "nudge" to buoyancy is required to match the geologically determined plate motions[15].

To investigate the temporal evolution of the AGL, we employ the quasi-reversibility (QRV) approach[47,] which reconstructs past temperature structures by integrating the governing equations of mantle dynamics backward in time. The QRV method has been successfully applied in previous studies to explore the long-term evolution of mantle plumes, subducted slabs, and other key features of Earth's interior[41,48]. Glišović & Forte[41] conducted extensive tests to evaluate the method's effectiveness for reconstructing mantle evolution over the Cenozoic Era (past 70 million years). They demonstrated that employing a time-dependent regularization parameter in the time-reversed energy conservation equation signifi antly enhances the method's robustness compared to one using a constant-value regularization parameter.

The uncertainties of the QRV method are quantifi d by comparing present-day geodynamic observables predicted by the method with observational datasets. Glišović & Forte[41] focused on predictions of free-air gravity anomalies, dynamic surface topography, and horizontal divergence. Their comparisons showed that, with a time-dependent regularization parameter, the QRV method reconstructs past mantle states with uncertainties, expressed in variance reduction, below 10% for these major observables over a timescale of 70 million years.

To further enhance the accuracy of our mantle reconstructions, we incorporated the QRV method in conjunction with a Back-and-Forth Nudging (BFN) technique, inspired by the nudging concept of Auroux & Blum[49]. The BFN technique, as developed and validated in Glišović & Forte[15], involves an iterative process that alternates between forward and backward integrations of the mantle convection model over a series of time windows. Specifically, the time interval over which we wish to reconstruct the evolution of the mantle (here, 70 Ma) is divided into discrete time windows bounded between a start time t_i and a finish time t_{i+1}, where time t increases positively into the past. All time windows span 2.5 Myr (i.e., t_{i+1}-t_i= 2.5 Myr), extending from 0 Ma to 70 Ma. In each time window, the temperature field at the start time T_j^s is iteratively updated/modified as follows:

$$T_j^s(t_i) = \begin{cases} T_0(t_i), & j = 1 \\ T_0(t_i) + W \sum_{j=2}^{n} \left(T_0(t_i) - T_{j-1}^p(t_i) \right), & j \geq 2, \end{cases} \quad (1)$$

where T_0 is the initial solution at the beginning of sequence, T_j^P is a prediction obtained by the direct (forward-in-time) integration of the preceding inverse (backward-in-time) solution at t_{i+1}, and W is a "nudging" multiplier for which the prescribed value is 0.75. This time-sequence iteration proceeds until the variance reduction between the prediction and the initial solution converges to a minimum value at the start time (typically at $j = 5$). On the final iteration, the reconstructed temperature field at the finish time is stored and employed as the starting condition for the next time window in the past. This iterative process reduces the cumulative errors associated with the QRV method, particularly those related to the smoothing effects of thermal diffusion. The BFN technique thus allows for the stable recovery of shorter wavelength features in the mantle, improving the overall resolution of mantle heterogeneity and leading to more precise reconstructions of the temperature and flow fields.

In our BFN framework, two classes of reconstructions are distinguished: the N (no-matching) and the M (matching). At each time step we apply a plate-geometry projection operator $\widehat{P}$ (dependent only on the plate masks and boundaries) to decompose internal buoyancy into two orthogonal families: $\widehat{\delta\rho} = \widehat{P}\,\delta\rho$ and $\overline{\delta\rho} = \delta\rho - \widehat{\delta\rho}$. $\widehat{\delta\rho}$ drives flow that is modelled with a purely free-slip surface boundary condition, and whose geometry is compatible with rigid, rotating surface plate motions. In contrast, $\overline{\delta\rho}$ produces a surface flow that is orthogonal to any possible rigid-plate motions and hence is modelled with a purely no-slip surface-boundary condition. In other words, the mantle flow driven by $\overline{\delta\rho}$ cannot produce any observable plate motions and the plates are "locked". The plate-projection operators depend only on plate geometry; they do not use, or fit to, plate velocities[24]. Geodynamic observables are then computed by convolving each buoyancy family with the appropriate free-slip/no-slip Green functions. Thus, plates organize how buoyancy drives motion, but do not prescribe motion in the N-model simulations: we do not assimilate any plate velocities. For the M-model simulations, we apply a small, instantaneous correction to the $\widehat{\delta\rho}$ buoyancy field (defined above) so that the predicted plate motions match geological estimates of past velocities: a minimum-norm update to the density anomalies[15].

This methodology for simulating plate-coupled mantle flow was originally described in Forte & Peltier[18]. These authors also showed that rigid-plate kinematics induces a linear coupling between the plate divergence (poloidal) and vorticity (toroidal) fields with coupling coefficients that depend only on plate geometry,in consequence, toroidal mantle flow is "driven from above" by rotating plates that are themselves driven by the buoyancy-induced poloidal flow below. In the N models, the plate-coupling is therefore geometric rather than a kinematic assimilation: plate shapes constrain (via the projection operator $\widehat{P}$) what parts of δρ can move plates, but plate velocities are never imposed.

The effectiveness of the BFN algorithm is demonstrated in Fig. S10, which shows the variance reduction fit between backward-in-time reconstructions and forward-in-time predictions of mantle temperature fields, evaluated at 2.5 Myr intervals over the past 70 million years. These results correspond to a model initialized with the GyPSuM tomography and the V1 viscosity profile and are computed over the full 3D temperature field – spanning all spherical harmonic degrees up to ℓ = 170 and all Chebyshev radial nodes (129). At each interval, the BFN constrains reconstruction-prediction mismatch to within 2% yielding variance reduction fits of at least 98%. The total accumulated mismatch – defined as the sum of all (100% minus variance reduction) values – remains ~24%, underscoring the method's ability to tightly control mismatch growth across the full integration window. This high level of round-trip fidelity confirms the internal consistency and numerical stability of the BFN framework for deep-time geodynamic reconstructions.

This robustness is further supported by comparisons between BFN-based forward predictions and observed present-day geodynamic signals, including plate motions, free-air gravity anomalies, dynamic surface topography, and CMB ellipticity. Glišović & Forte[15] demonstrated that mantle heterogeneity reconstructed at 70 Ma yields, upon forward integration, a present-day configuration that achieves excellent quantitative fits to these observables across a wide spectral range (harmonic degrees ℓ= 1–32).

These fits to a diverse set of present-day geodynamic observables serve as a critical benchmark for assessing the reliability of the BFN reconstructions and their capacity to predict the time-dependent evolution of geoid anomalies. In this context, we define the "initial" model as the tomography-based inference of present-day mantle heterogeneity used to initialize the BFN algorithm. The algorithm then reconstructs the mantle structure backward to 70 Ma, from which a forward-in-time simulation generates a "prediction" of present-day structure. This predicted field is quantitatively compared against both the initial model and observed geoid anomalies, allowing for rigorous evaluation of internal consistency and predictive accuracy.

The predicted nonhydrostatic geoid reflect the combined contributions of internal mantle density anomalies and geopotential perturbations arising from flow-induced dynamic topography at both the solid-surface and core-mantle boundary. These predictions fully account for self-gravitational effects in a compressible Earth

model via viscous-fl w Green's functions. Surface dynamic topography is computed with feedback from the plate-like mechanical boundary condition, which enforces a mixed free-slip and no-slip behaviour, as detailed by Forte[25].

Variance reduction analysis (Table S1) shows that the initial GyPSuM-V1-N model yields a 91% fit to the observed nonhydrostatic geoid, indicating strong agreement between the tomography-derived anomalies and present-day geoid undulations. Th s high fit underscores the robustness of the GyPSuM model combined with the V1 viscosity profile under the no-matching (N) plate velocity condition, validating its use as a starting configur tion for backward convection modelling. The predicted geoid from the GyPSuM-V1-N model achieves an 85% fit to the observed nonhydrostatic geoid (Table S1), refl cting strong predictive capability despite the inherent difficulty of recovering past mantle structure. The predicted geoid also retains a 93% fit to its initial configur tion (i.e., GyPSuM-V1-N at present day), underscoring the internal consistency and stability of the BFN algorithm. The prediction based on the GyPSuM-V1-M model yields an 87% fit to the observed geoid (Table S1), slightly exceeding the performance of the GyPSuM-V1-N case and demonstrating excellent compatibility with the surface plate motions. The corresponding fit between the prediction and its initial model is 94%, further affirming the reliability and predictive strength of the BFN method when applied with a matching-velocity constraint.

The robustness documented above is not limited to GyPSuM + V1 only: across all tested tomography-viscosity combinations, the BFN framework consistently reproduces the initial present-day geoid with variance reductions exceeding 93% (Table S1). Th s consistency clearly underscores the BFN framework's reliability as a numerical method, independent of the particular initial condition employed. However, the choice of initial conditions remains critical, as it sets the density structure that generates the predicted geoid anomalies. It is for this reason that we systematically tested different tomography-viscosity combinations to evaluate their fit to the observed geoid anomalies.

Variance reduction values for alternative mantle convection models – based on different combinations of tomography inputs and viscosity profiles – are presented in Table S1 and discussed in the Supplementary Section "3". These include models using independent viscosity inferences from Steinberger & Calderwood[50] and density anomalies derived from the S40RTS tomography model[44]. Overall, these variance reduction values provide important insights into the performance of different mantle convection reconstructions and their predictive power.

In the detailed sensitivity and uncertainty analysis presented in the Supplementary Material (Section "2"), we show that time-dependent geoid predictions remain stable across a range of plausible mantle viscosity profiles and different tomography inputs. While variations in viscosity structure and tomography model influence the amplitude of the AGL anomaly, the temporal trends and key evolutionary features are largely insensitive to these choices. Specifi ally, despite model-dependent differences in magnitude and rate of change, all reconstructions consistently capture a pronounced transition in the AGL evolution between 50 and 30 Ma (Fig. S2**b**), underscoring the robustness of this timing, even as the amplitude trajectories differ across models.

To independently assess the realism and accuracy of our mantle convection reconstructions, we conducted a critical validation test based on their ability to reproduce TPW trajectories inferred from paleomagnetic data over the past 70 million years (Section 5 in the Supplementary Material). TPW, which represents the time-dependent shifts of Earth's rotation axis, can be inferred from paleomagnetic data and it provides a stringent external constraint on Earth's rotational stability and on the long-wavelength dynamics of mantle density anomalies expressed in changes to the moment of inertia tensor that are directly mapped by the coeffici ts in the time-dependent degree-2 geoid. As shown in Fig. S3 and Table S2, our time-dependent convection models closely reproduce key features of the paleomagnetic inferred TPW path, including abrupt changes in direction and a prominent U-turn near 50 Ma. Th s alignment supports the physical realism of our predicted AGL evolution, which is governed by mantle buoyancy and viscosity structure, and confi ms the self-consistency of the numerical solution.

The intrinsic nonlinearity of mantle convection, via the advection of temperature term in the conservation of energy equation, ensures coupling between all harmonic degrees of mantle temperature and fl w structure (Sections 6 & 7 in Supplementary Material). Consequently, matching the degree-2 component of the geoid – as required by TPW – is not an isolated achievement. While this match does not by itself ensure accurate fits to the higher degree geoid components, it nonetheless establishes confide ce in the dynamical consistency of the temporal evolution of higher-degree harmonics in the mantle buoyancy fi ld (and hence to their surface gravitational expression) that are nonlinearly coupled to the changes in degree-2 buoyancy and corresponding geoid anomalies. Thus, the successful fit to TPW, and therefore the corresponding degree-2 geoid evolution, provides a fundamental dynamic verifi ation of the 4-D evolution of our mantle reconstructions, reinforcing the dynamic credibility of the full spectral structure of the predicted geoid fi ld.

Following Glišović & Forte[22], we further examined the reconstructed mantle fl w by computing trajectories of passive particles advected through the time-dependent velocity fi ld. Th s was done using an eighth-order Dormand-Prince Runge-Kutta integrator[51] applied to the spectrally resolved fl w fi ld, where horizontal and radial variations are expressed in spherical harmonic and Chebyshev expansions, respectively. Th s spectral representation permits precise evaluation of fl w velocities at arbitrary spatial locations, avoiding interpolation-induced numerical artifacts. Fig. S9 shows the initial and fi al positions of whole-mantle trajectories that originate at the top of the seismic D" layer (250 km above the CMB) and terminate in the transition zone (500 km depth) beneath the Ross Sea and hence under the AGL. We assume that mantle fl w remains approximately steady before 70 Ma, based on the observation that all tracers reside in the lower mantle before this time, where the high viscosity stabilizes fl w patterns. Th s long-term coherence of deep mantle fl w – refl cting the persistence of thermochemical upwellings – was analyzed in detail by Glišović & Forte[52].

Data availability

All data used in this study to generate results have been previously published in the cited references. Additional results/data related to this paper are available from the corresponding author, PG.

Code availability

The executable code that supports the fi dings of this study is available from the corresponding author, PG. All numerical methods applied in this code have been previously published in the cited references.

Received: 17 June 2025; Accepted: 11 November 2025
Published online: 19 December 2025

References

1. Lemoine, F. G. et al. New high resolution model developed for Earth's gravitational fi ld. *Eos, Trans. Am. Geophys. Union* **79**(9), 113–118 (1998).
2. Tapley, B. D., Bettadpur, S., Watkins, M. & Reigber, C. The gravity recovery and climate experiment: Mission overview and early results. *Geophys. Res. Lett.* **31**(9), L09607 (2007).
3. Decker, B. L. World geodetic system 1984. Defense mapping agency aerospace center St Louis Afs Mo; https://apps.dtic.mil/sti/tr/pdf/ADA167570.pdf (1986).
4. Spasojevic, S., Gurnis, M. & Sutherland, R. Mantle upwellings above slab graveyards linked to the global geoid lows. *Nat. Geosci.* **3**(6), 435–438 (2010).
5. Pal, D. & Ghosh, A. How the Indian Ocean geoid low was formed. *Geophys. Res. Lett.* **50**(9), e2022GL102694 (2023).
6. Chambat, F., Ricard, Y. & Valette, B. Flattening of the earth: Further from hydrostaticity than previously estimated. *Geophys. J. Int.* **183**(2), 727–732 (2010).
7. Richards, M. A. & Engebretson, D. C. Large-scale mantle convection and the history of subduction. *Nature* **355**(6359), 437–440 (1992).
8. Panet, I. et al. Mapping the mass distribution of Earth's mantle using satellite-derived gravity gradients. *Nat. Geosci.* **7**(2), 131–135 (2014).
9. Dziewonski, A. M., Hager, B. H. & O'Connell, R. J. Large-scale heterogeneities in the lower mantle. *J. geophys. Res.* **82**, 239–255 (1977).
10. Hager, B. et al. Lower mantle heterogeneity, dynamic topography and the geoid. *Nature* **313**, 541–545. https://doi.org/10.1038/313541a0 (1985).
11. Richards, M. A. & Hager, B. H. The Earth's geoid and the large scale structure of mantle convection. In *The Physics of Planets* (ed. Runcorn, S. K.) 247–272 (John Wiley, 1988).
12. King, S. D. & Masters, G. An inversion for radial viscosity structure using seismic tomography. *Geophys. Res. Lett.* **19**(15), 1551–1554 (1992).
13. Forte, A. M., Dziewonski, A. M., & Woodward, R. L. Aspherical structure of the mantle, tectonic plate motions, nonhydrostatic geoid, and topography of the core-mantle boundary. In *Dynamics of Earth's deep Interior and Earth rotation* AGU Geophysical Monograph **72** 135 166 (1993).
14. Chase, C. G. & Sprowl, D. R. The modern geoid and ancient plate boundaries. *Earth Planet. Sci. Lett.* **62**, 314–320 (1983).
15. Glišović, P. & Forte, A. M. A new back-and-forth iterative method for time-reversedconvection modelling: Implications for the Cenozoic evolution of 3-D structure anddynamics of the mantle. *J. Geophys. Res. Solid Earth* **121**, 1–18 (2016).
16. Glišović, P., Forte, A. M. & Moucha, R. Time-dependent convection models of mantle thermalstructure constrained by seismic tomography and geodynamics: Implications for mantle plume dynamics andCMB heat flux. *Geophys. J. Int.* **190**(2), 785–815 (2012).
17. Rowley, D. B. et al. Kinematics and dynamics of the East Pacific rise linked to a stable, deep-mantle upwelling. *Sci. Adv.* **2**(12), e1601107 (2016).
18. Forte, A. M. & Peltier, W. R. The kinematics and dynamics of poloidal-toroidal couplingin mantle fl w: The importance of surface plates and lateral viscosity variations. *Adv. Geophys.* **36**, 1–119 (1994).
19. Mitrovica, J. X. & Forte, A. M. A new inference of mantle viscosity based upon jointinversion of convection and glacial isostatic adjustment data. *Earth Planet. Sci. Lett.* **225**, 177–189 (2004).
20. Forte, A. M. et al. Joint seismic–geodynamic-mineral physical modelling of African geodynamics: A reconciliation of deep-mantle convection with surface geophysical constraints. *Earth Planet. Sci. Lett.* **295**(3–4), 329–341 (2010).
21. Glišović, P. & Forte, A. M. On the deep-mantle origin of the Deccan Traps. *Science* **355**, 613–616 (2017).
22. Glišović, P. & Forte, A. M. Two deep-mantle sources for Paleocene doming and volcanism in the North Atlantic. *Proc. Natl. Acad. Sci.* **116**(27), 13227–13232 (2019).
23. Simmons, N. A., Forte, A. M., Boschi, L. & Grand, S. P. GyPSuM: A joint tomographicmodel of mantle density and seismic wave speeds. *J. Geophys. Res. Solid Earth* **115**, B12310 (2010).
24. Forte, A. M., Simmons, N. A. & Grand, S. P. Constraints on 3-D seismic models fromglobal geodynamic observables: Implications forthe globalmantle convective fl w. In *Treatise on Geophysics* 2nd edn, Vol. 1 (eds Dziewonski, A. M. & Romanowicz, B.) 853–907 (Elsevier, 2015).
25. Forte, A. Constraints on seismic models from other disciplines—Implications for mantle dynamics and composition. In *Treatise onGeophysics* 1st edn, Vol. 1 (eds Dziewonski, A. M. & Romanowicz, B.) 805–858 (Elsevier, 2007).
26. Liu, X. & Zhong, S. Constraining mantle viscosity structure for athermochemical mantle using the geoid observation. *Geochem. Geophys. Geosyst.* **17**, 895–913. https://doi.org/10.1002/2015GC006161 (2016).
27. Liu, S. & King, S. D. Dynamics of the north american plate: Large-scale driving mechanism from far-fi ld slabs and the interpretation of shallow negative seismic anomalies. *Geochem. Geophys. Geosyst.* **23**(3), 808 (2022).
28. Merdith, A. S. et al. Extending full-plate tectonic models into deep time: Linking the Neoproterozoic and the Phanerozoic. *Earth-Sci. Rev.* **214**, 103477 (2021).
29. Faccenna, C. et al. Role of dynamic topography in sustaining the Nile River over 30 million years. *Nat. Geosci.* **12**(12), 1012–1017 (2019).
30. Van der Meer, D. G., Van Hinsbergen, D. J. & Spakman, W. Atlas of the underworld: Slab remnants in the mantle, their sinking history, and a new outlook on lower mantle viscosity. *Tectonophysics* **723**, 309–448 (2018).
31. Riley, T. R., Burton-Johnson, A., Hogan, K. A., Carter, A. & Leat, P. T. Cretaceous–Paleogene tectonic reconstructions of the South Scotia Ridge and implications for the initiation of subduction in the Scotia Sea. *J. Geol. Soc.* **180**(4), jgs2023-013 (2023).
32. Schellart, W. P., Strak, V., Beniest, A., Duarte, J. C. & Rosas, F. M. Subduction invasion polarity switch from the Pacific to the Atlantic Ocean: A new geodynamic model of subduction initiation based on the Scotia Sea region. *Earth Sci. Rev.* **236**, 104277 (2023).
33. Rowley, D. B. Extrapolating oceanic age distributions: Lessons from the Pacific egion. *J. Geol.* **116**(6), 587–598 (2008).

34. Bredow, E., Steinberger, B., Gassmöller, R. & Dannberg, J. Mantle convection and possible mantle plumes beneath Antarctica–insights from geodynamic models and implications for topography. *Geol. Soc. London Mem.* **56**(1), 253–266 (2023).
35. Panter, K. S. Chapter 1.3 Antarctic volcanism: Petrology and tectonomagmatic overview. *Geol. Soc. London Mem.* **55**(1), 43–53 (2021).
36. Ferraccioli, F. et al. East Antarctic rifting triggers uplift of the Gamburtsev Mountains. *Nature* **479**, 388–392. https://doi.org/10.1038/nature10566 (2011).
37. Williams, S. E., Whittaker, J. M., Halpin, J. A. & Müller, R. D. Australian-Antarctic breakup and seafl or spreading: Balancing geological and geophysical constraints. *Earth-Sci. Rev.* **188**, 41–58 (2019).
38. Farrell, W. E. & Clark, J. A. On postglacial sea level. *Geophys. J. Int.* **46**, 647–667 (1976).
39. Paxman, G. J. Antarctic palaeotopography. *Geol. Soc. London Mem.* **56**(1), 231–251 (2023).
40. Austermann, J. & Mitrovica, J. X. Calculating gravitationally self-consistent sea level changes driven by dynamic topography. *Geophys. J. Int.* **203**(3), 1909–1922 (2015).
41. Glišović, P. & Forte, A. M. Reconstructing the Cenozoic evolution of the mantle: Implications for mantle plume dynamics under the Pacific nd Indian plates. *Earth Planet. Sci. Lett.* **390**, 146–156 (2014).
42. Simmons, N. A. "Mantle heterogeneity and fl w from seismic and geodynamic constraints." Doctoral Dissertation. The University of Texas at Austin, 255pp. https://repositories.lib.utexas.edu/bitstreams/f615e0e1-2503-4e21-8e0b-372766f f950/download (2007).
43. Glišović, P., Grand, S. P., Lu, C., Forte, A. M. & Wei, S. S. The effects of discontinuity topography in the mantle transition zone on global geodynamic observables and mantle heterogeneity. *Geophys. J. Int.* **230**(1), 623–642 (2022).
44. Ritsema, J., Deuss, A., Van Heijst, H. J. & Woodhouse, J. H. S40RTS: A degree-40 shear-velocity model for the mantle from new Rayleigh wave dispersion, teleseismic traveltime and normal-mode splitting function measurements. *Geophys. J. Int.* **184**(3), 1223–1236 (2011).
45. Katsura, T., Yamada, H., Nishikawa, O., Song, M., Kubo, A., Shinmei, T., ... & Funakoshi, K. I.Olivine wadsleyite transition in the system (Mg, Fe) 2SiO4. *J. Geophys. Res.: Solid Earth* **109**(B2), (2004).
46. Glišović, P., Forte, A. M. & Ammann, M. W. Variations in grain size and viscosity based on vacancy diffusion in minerals, seismic tomography, and geodynamically inferred mantle rheology. *Geophys. Res. Lett.* **42**(15), 6278–6286 (2015).
47. Lattès, R. & Lions J.-L., The method of quasi-reversibility: Applications to partial differential equations. (Translated from French) 388 (American Elsevier Pub. Co., New York, 1969).
48. Ismail-Zadeh, A., Korotkii, A., Schubert, G. & Tsepelev, I. Quasi-reversibilitymethod for data assimilation in models of mantle dynamics. *Geophys. J. Int.* **170**, 1381–1398 (2007).
49. Auroux, D. & Blum, J. Back and forth nudging algorithm for data assimilation problems. *Comptes Rendus. Math.* **340**(12), 873–878 (2005).
50. Steinberger, B. & Calderwood, A. R. Models of large-scale viscous fl w in the Earth's mantle with constraints from mineral physics and surface observations. *Geophys. J. Int.* **167**(3), 1461–1481 (2006).
51. Hairer E, Norsett SP, Wanner G. In *Solving Ordinary Differential Equations I. Nonstiff Problems*. 2nd Eds (Springer series in computational mathematics, Springer-Verlag, 1993).
52. Glišović, P. & Forte, A. M. Importance of initial buoyancy fi ld on evolution of mantle thermal structure: Implications of surface boundary conditions. *Geosci. Front.* **6**(1), 3–22 (2015).

Acknowledgments

The authors acknowledge the support provided by the French "Programme d'investissements d'avenir" under the auspices of the GYPTIS project – ANR 19 MPGA 0007 and the support provided by the Institut de Physique du Globe de Paris. PG acknowledges support from Queen's University and the support of this work provided by the Stephen Cheeseman Geoselenic Research Project. AMF acknowledges support from the University of Florida and the support of this work provided by NSF grant EAR 1903108. The authors also acknowledge the additional support provided by GEOTOP, Université du Québec à Montréal. The authors thank Pavel Dubrovin and Bernhard Steinberger for providing data and supporting material for the paleomagnetic inferences of TPW trajectories presented in Figure 10 of their paper (Doubrovine et al., 2012), which is discussed and referenced in the Supplementary Material. The authors want to thank a number of colleagues for extensive discussions related to mantle dynamics, surface geological evolution, and Earth's geoid: Stephen Grand, Nathan Simmons, David Rowley (deceased in 2024), Shangxin Liu, Marianne Greff, Shayan Kamali Lima and Alexander Braun. Their longstanding encouragement and support of our work is gratefully acknowledged. The convection simulations in this study were carried out thanks to supercomputing facilities of Digital Research Alliance of Canada and University of Florida. PG and AMF both developed the scientific concept and modelling techniques presented here and jointly wrote the paper.

Author contributions

PG and AMF both developed the scientific concept and modelling techniques presented here and jointly wrote the paper.

Funding

Th s work was funded by the French "Programme d'investissements d'avenir" under the GYPTIS project – ANR 19 MPGA 0007 at the Institut de Physique du Globe de Paris. PG is additionally supported by the Stephen Cheeseman Geoselenic Research Project at Queen's University. AMF acknowledges support from the University of Florida and the support of this work provided by NSF grant EAR 1903108.

Declarations

Competing interests

The authors declare no competing interests.

Additional information

Supplementary Information The online version contains supplementary material available at https://doi.org/10.1038/s41598-025-28606-1.

Correspondence and requests for materials should be addressed to P.G.